Molecular Catalysis 457 (2018) 1–7

Contents lists available at ScienceDirect

Molecular Catalysis

journal homepage: www.elsevier.com/locate/mcat

Tuning of oxygen species and active Pd^{2+} species of supported catalysts via morphology and Mn doping in oxidative carbonylation of phenol

Xiaojun Yang[a,b], Yue Hu[a], Hang Bai[a], Maoqi Feng[c], Zhiguo Yan[a,*], Shuo Cao[a,*], Bin Yang[b,*]

[a] Key Laboratory for Green Chemical Process of Ministry of Education, School of Chemical Engineering and Pharmacy, Wuhan Institute of Technology, Wuhan 430205, PR China

[b] Bioproduct Sciences and Engineering Laboratory, Department of Biological Systems Engineering, Washington State University, Richland, WA 99354, USA

[c] Chemistry & Chemical Engineering Division, Southwest Research Institute, San Antonio, TX 78238, USA

ARTICLE INFO

Keywords:
Morphology
Dopants
Oxygen species
Oxidative carbonylation
Ceria

ABSTRACT

A series of nanocubes and nanorods of CeO_2 and Mn_xCe_yO (x,y = 1 or 3) oxides were prepared by the hydrothermal method. Samples as prepared were characterized by Transmission electron microscopy, X-ray diffraction, X-ray photoelectron spectroscopy and Raman spectroscopy, in order to gain a fundamental understanding of the effects of the morphology and Mn dopant on the oxygen species and active Pd^{2+} species in the oxidative carbonylation of phenol using Pd catalysts supported on as-prepared oxides. Although the oxygen species on supports with different morphologies varied, the catalytic performance in the oxidative carbonylation reaction did not show the significant change. Comparatively speaking, the doping of Mn is a more efficient method to control active oxygen species. It is deduced that Pd and Mn are "dopants" for pure CeO_2, both of which improve the formation of oxygen vacancies that help to mitigate the reduction of active Pd species due to the strong interaction between the Pd^{2+} and the Mn_xCe_yO support. Furthermore, we propose that O_β (hydroxyl oxygen, chemisorbed oxygen or the oxygen vacancy) species acted as intermediates to lower the reduction of active palladium species by the strong interaction between the noble metal and supports, while the lattice oxygen O_α were involved in the redox cycle of Pd^0/Pd^{2+} in the oxidative carbonylation of phenol to diphenyl carbonate. All results suggest that Mn dopants play a more important role in the activity than morphology does.

1. Introduction

Diphenyl carbonate (DPC) can be utilized to synthesize many important organic compounds and polymer materials [1,2]. For example, DPC reacts with bisphenol-A to produce polycarbonate, which is widely employed as an engineering plastic. The synthesis of DPC includes the traditional phosgene method, the transesterification process of phenol and aliphatic carbonate, and the oxidative carbonylation of phenol [3,4]. Among them, the oxidative carbonylation of phenol to produce DPC has gained more and more attention due to more stringent environmental policy all over the world [5]. Phenol reacts with CO and O_2, as shown in Eq. (1), to produce DPC and water in the presence of palladium catalysts. During this process, the use of highly toxic phosgene can be avoided and water is the sole byproduct.

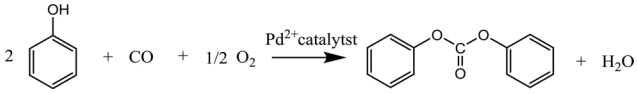

(1)

As research continues, the catalyst efficiency for the oxidative carbonylation reaction has been improved to a certain extent [6]. Homogeneous palladium catalysts $PdCl_2$, $Pd(OAC)_2$, $Pd(acac)_2$, Pd-carbene complex [7] and Pd-2,2′-bipyridyl complex [8] have been used for the oxidative carbonylation of phenol over the past few decades. Recently, heterogeneous palladium-supported catalysts have attracted more and more attention, and heterogeneous palladium catalysts anchored on various supports including activated carbon [9], polystyrene [10], silicon dioxide [11], layered double hydroxides [12], organic-inorganic hybrid materials [13] and mixed metal oxides [14,15] were extensively investigated. However, the catalyst performance is unable to meet the requirements of commercialization until now because of the fast deactivation (short lifetime) of the catalysts, which could be caused by the reduction of active palladium species during the oxidative carbonylation reaction. Therefore, it is critical to seek the solution(s) to prevent the reduction of palladium species [16]. Furthermore, it has been found that solely gaseous oxygen (O_2) is less effective at re-oxidizing the reduced palladium species than the combination of gaseous oxygen with

* Corresponding authors.
E-mail addresses: samanyan@163.com (Z. Yan), cao23@email.sc.edu (S. Cao), bin.yang@wsu.edu (B. Yang).

https://doi.org/10.1016/j.mcat.2018.07.004
Received 8 January 2018; Received in revised form 12 June 2018; Accepted 2 July 2018

the other types of oxygen species (lattice oxygen or surface oxygen) [17].

In addition to gaseous oxygen, it is necessary to verify the role of other oxygen species in the catalytic reaction. Oxygen species are proven to play a vital catalytic role in low-temperature CO oxidation, the oxidative coupling of methane, the removal of volatile organic compounds and the purification automotive exhaust gas, etc. [18]. As for oxidation carbonylation of phenol, we proposed in our previous study that 1) the formation of more OH^- group, a type of oxygen species, is more beneficial to the redox cycle between active Pd species and supports, and 2) the nature of oxygen species on the surface of a catalyst strongly depends on the metal cation (Pb^{2+}) [19]. To our best knowledge, metal doping is a typical method to alter the oxygen species in oxides. Recently, another strategy of tuning the oxygen species of catalytic material via the morphology effect in microscopic scale was reported [20–22]. Many researches have been done on the effect of morphology on metal oxide catalysts in catalytic performance, such as CeO_2, MnO_x-CeO_2 mixed oxides, etc. [23,24]. The catalytic properties of metal oxide catalysts were attributed to specific crystal planes exposed on nanocrystals with different morphology, such as the (100) planes and (110) planes exposed in cubic and rod-like CeO_2, respectively. This is because the lattice oxygen species on the (100) planes have a higher mobility than that on the (110) plane in CeO_2 [23]. Furthermore, the strong morphology-induced effect of CeO_2 on the active Pt species was observed during CO oxidation, where three morphological types of CeO_2 (cube, rod and octahedral) were employed as supports [25]. Therefore, it is essential to investigate the morphological effect of nanocatalysts and verify the role of oxygen species in the catalytic cycle of active palladium species, which would give an insight into the development of catalysts with high and stable performance.

Our research groups focused on the synthesis of Perovskite and Cryptomelane-type metal oxides as the supports for palladium catalysts [15,17,26,27]. We note that less attention is paid to the morphology of heterogeneous catalysts in the present study on the oxidative carbonylation of phenol. Herein, CeO_2 and Mn_xCe_yO mixed oxides with various morphologies were obviously synthesized by the hydrothermal method as the supports for palladium catalysts. We hope that the research on these morphological effects will provide a comparable quantitative means of deepening the fundamental understanding of the role of oxygen species in catalytic oxidative carbonylation reaction. Moreover, the interaction mechanism between the metal oxide supports and active palladium species will be explored further. Compared with morphological tuning, Mn doping was adopted to establish a more clear relationship among the oxygen species and active Pd species in terms of catalytic performance.

2. Experiments

2.1. Sample preparation

Both CeO_2 and MnO_x–CeO_2 nanomaterials were prepared under hydrothermal conditions as supports.

CeO_2 nanocubes were synthesized with a $Ce(NO_3)_3{\cdot}6H_2O$ aqueous solution(3.00 g, 10 ml) and a NaOH aqueous solution (16.88 g,70 ml). The above two aqueous solutions were mixed, introduced into an autoclave, and kept at 453 K for 24 h. The precipitate from the autoclave was filtered, washed, and dried at 333 K for 6 h, and finally calcined at 673 K for 3 h. The solid obtained was denoted as CeO_2-cubes.

CeO_2 nanorods were synthesized with a $CeCl_3{\cdot}7H_2O$ aqueous solution (2.99 g, 80 ml) and NaOH (38.41 g, 80 ml). The synthetic procedure of nanocubes was similar to that of the nanorods. The temperature of the autoclave was 423 K for 12 h, and the calcination temperature was 573 K for 3 h. CeO_2 nanorods are marked as CeO_2-rods.

Different amounts of $Mn(NO_3)_2$ and $MnCl_2$ were added to prepare MnO_x-CeO_2 mixed oxides with the morphology of cubes and rods based on the preparation method of pure CeO_2. The samples with the particular molar ratios of Mn to Ce of 1/3, 1/1 and 3/1 in the shape of either cubes or rods were labeled as Mn_1Ce_3O-cube, Mn_1Ce_1O-cube, Mn_3Ce_1O-cube, Mn_1Ce_3O-rod, Mn_1Ce_1O-rod, and Mn_3Ce_1O-rod, respectively.

The detailed palladium-loaded procedure of the precipitation method is as follows: $PdCl_2$ (0.42 g) was firstly dissolved in 50.0 ml of aqueous solution and the pH was subsequently adjusted to 1.0 with concentrated hydrochloric acid. The CeO_2 and MnO_x–CeO_2 supports (5.0 g) were then impregnated with the above $PdCl_2$ solution. Following that, the precipitating agent, NaOH solution (3 mol/L), was added dropwise into the above slurry until the pH value was 9–10. Finally, the supported palladium catalysts were separated by filtration and washed with distilled water several times. They were then dried at 333 K and calcined at 573 K for 3 h. The palladium supported catalysts are denoted as Pd/Mn_xCe_yO(x,y = 1 or 3) corresponding to the supports.

2.2. Characterization

X-ray Diffraction (XRD) patterns were recorded on a D8 Advance (Bruker, Germany) diffractometer using Cu Kα radiation operated at 40 kV and 200 mA, with 2θ from 10° to 80°.

Transmission Electron Microscope (TEM) images were conducted on a JEM-2100 (JEOL, Japan) operated at 200 kV, and high-resolution TEM (HRTEM) images were taken on a FEI Tecnai G2 F30 microscope operated at 300 kV. The specimen was prepared by ultrasonically dispersing the sample powder in ethanol, and droplets of the suspension were deposited on a carbon-coated copper grid and dried in air. Energy dispersive X-ray spectroscopy (EDX/EDS) was used to determine the chemical composition of the samples.

X-ray Photoelectron Spectroscopy (XPS) analysis was carried out on a K-Alpha XPS instrument (Thermo Fisher Scientific, America), employing Al- Kα radiation. The binding energy (BE) for the samples was calibrated by setting the measured BE of C 1s to 284.6 eV.

Raman Spectra were measured at room temperature using a DXR Raman microscope (Thermo Fisher Scientific, America) with a 514.5 nm excitation source from an Ar^+ laser.

Brunaur Emmett Teller (BET) nitrogen adsorption plots were used to measure the change in the specific surface area of the catalysts on a Nova 2000e surface area and pore size analyzer (Quantachrome Instruments, America).

2.3. Catalytic evaluation

The oxidative carbonylation reaction was performed in a 250 ml stainless steel autoclave equipped with a magnetic stirrer to facilitate external mass transfer. Phenol 47 g (0.5 mol), tetrabutylammonium bromide (TBAB) 1 g (3 mmol), and Pd (in the catalyst) 0.47 mmol were introduced into the autoclave. Then, the autoclave was sealed and heated to 65 °C. Subsequently, the gas mixture of CO and O_2 (CO/O_2 = 12/1 M ratio) became charged. After the reaction lasted for 4 h at the pressure of 4.8 MPa, the autoclave was cooled and the products were taken out. The final products were determined by capillary gas chromatography. The activity tests were carried out under a kinetic regime without the impact of mass transfer limitations.

3. Results and discussion

3.1. Morphological effects of oxide supports

The morphology of synthesized metal oxide supports was characterized by TEM, the images of which are shown in Fig. 1. The doping of Mn did not result in a change in morphology for neither nanocubes nor nanorods (Fig. 1(a)–(d)). A subtle difference that was present was that the surface of Mn_1Ce_3O-cube (Fig. 1(c)) appeared rougher and their corners were rounder than that of pure CeO_2-cube (Fig. 1(a)).

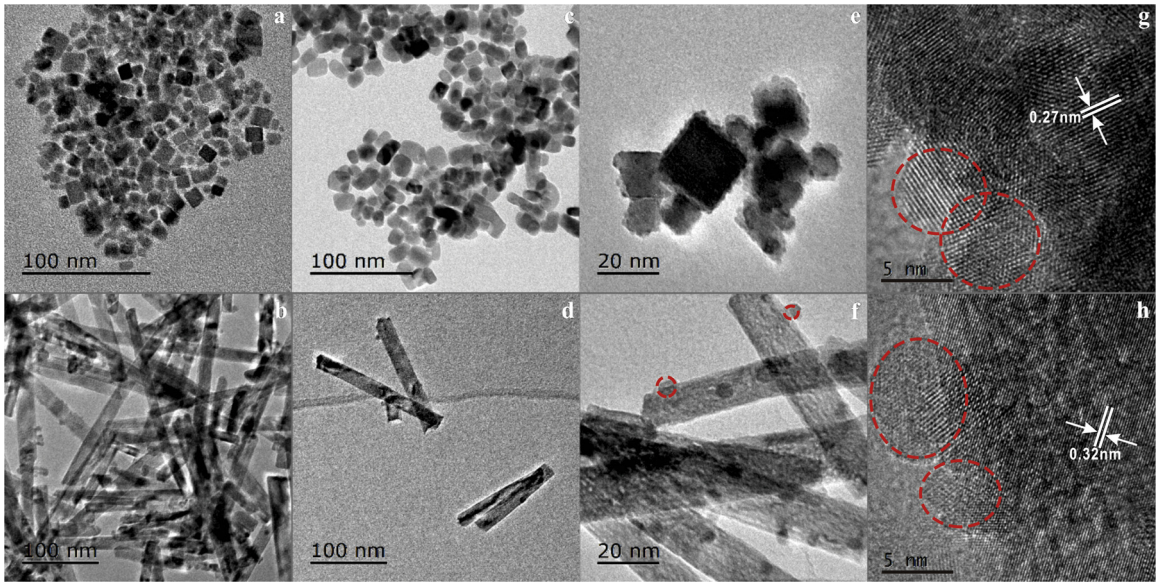

Fig. 1. TEM images of supports and Pd supported catalysts. (a) CeO_2-cube, (b) CeO_2-rod, (c) Mn_1Ce_3O-cube, (d) Mn_1Ce_3O-rod, (e) Pd/CeO_2-cube, (f) Pd/CeO_2-rod, (g)Pd/ Mn_1Ce_3O-cube, (h) Pd/ Mn_1Ce_3O-rod. The palladium particles were marked by the red cycles. (For interpretation of the references to color in this figure legend, the reader is referred to the web version of this article).

Furthermore, (100) crystal planes and (111) crystal planes were selectively exposed in CeO_2 nanocubes and CeO_2 nanorods, and the crystalline interplanar spacing of nanocubes and nanorods were 0.27 nm and 0.32 nm, respectively, which is consistent with what the literature reported (Fig. S1(a) and (b), respectively) [28]. Fig. 1(e) and (f) showed that palladium particles were well deposited on the surface of CeO_2-cube and CeO_2-rod supports. The original morphology of the CeO_2 or Mn_1Ce_3O support was well preserved even after the loading of Pd. The palladium particles were well dispersed on the surface of the CeO_2 and Mn_1Ce_3O nanorods (Fig. 1(f), (h)), whereas palladium particles came close together around the supports of the CeO_2 and Mn_1Ce_3O nanotubes (Fig. 1(e), (g)). The particle size of palladium species on the surface of CeO_2-cube was indistinguishable due to the overlap of Pd particles, which made it difficult to count the particle size from the TEM images. Herein, the Pd particle size in Pd/CeO_2-rod was estimated to be in the range of 6 nm–10 nm. Seen from Fig. 1(g) and (h), the Pd particle size for Pd/Mn_1Ce_3O-cube and Pd/Mn_1Ce_3O-rod also falls within this range.

Fig. 2 shows the XRD patterns of both the supports and the supported palladium catalysts. All diffraction peaks can be well indexed to the typical cubic fluoride CeO_2 crystal phase (JCPDS No. 34-0394). Neither manganese oxides nor the palladium species were observed from the XRD patterns. This indicates good incorporation of Mn into the crystal lattice to form solid solutions. Moreover, the lack of diffraction peaks related to palladium species means that the palladium particles were highly dispersed, which highly agrees with TEM images. The slight shift of the diffraction peak declares that manganese species entered into the ceria lattice with the formation of solid solutions. The lattice constant of *a* was calculated as equal to 0.5416 nm (CeO_2-cube), 0.5405 nm (Mn_1Ce_3O-cube), 0.5411 nm (CeO_2-rod), and 0.5398 nm (Mn_1Ce_3O-rod). It can be seen that lattice constant of *a* decreases with the addition of Mn for either cube and rod samples, suggesting that Mn^{n+} ions are incorporated into the ceria lattice to form a solid solution, since the radius of Mn^{n+} ion (Mn^{2+}: 0.083 nm, Mn^{3+}: 0.065 nm, Mn^{4+}: 0.053 nm) is smaller than that of the Ce^{n+} (Ce^{3+}: 0.103 nm; Ce^{4+}: 0.092 nm).

Based on the successful morphology-controlled synthesis of oxides, the oxygen species was studied by XPS spectra and Raman spectroscopy. Fig. 3 shows the O1s XPS spectra of CeO_2 and Mn_1Ce_3O supports and supported Pd catalysts with cubic and rod-like shapes. O_α species at lower binding energy of about 527 eV–529 eV can be ascribed to the

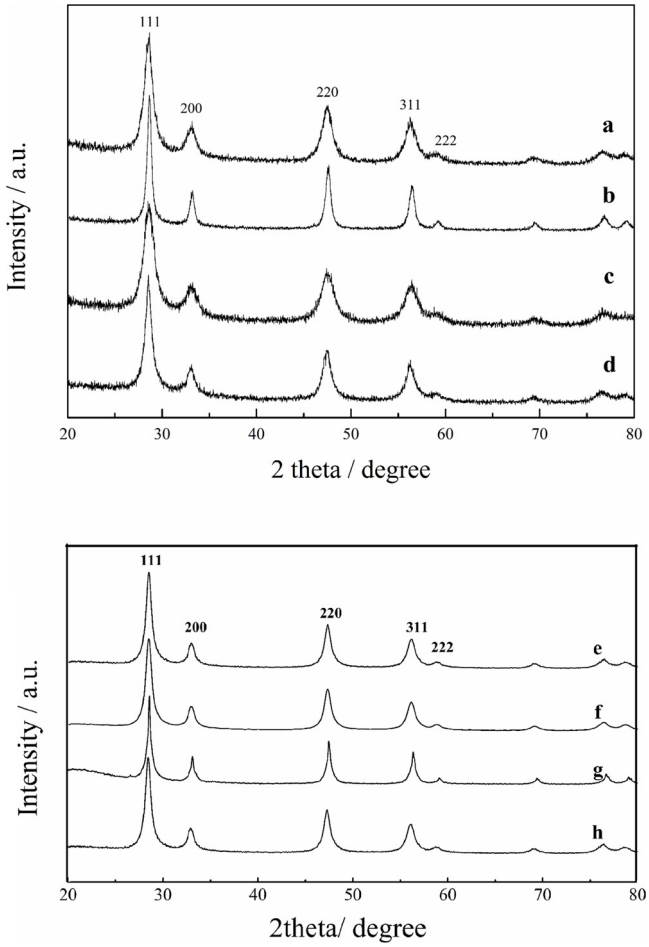

Fig. 2. XRD patterns of (a) CeO_2-cube, (b) CeO_2-rod, (c) Mn_1Ce_3O-cube, (d) Mn_1Ce_3O-rod (e) Pd/CeO_2-cube, (f) Pd/CeO_2-rod, (g) Pd/Mn_1Ce_3O-cube and (h) Pd/Mn_1Ce_3O-rod.

lattice oxygen, and another peak at higher binding energy ranging from 530 eV to 532 eV, O_β species, is assigned to the hydroxyl oxygen,

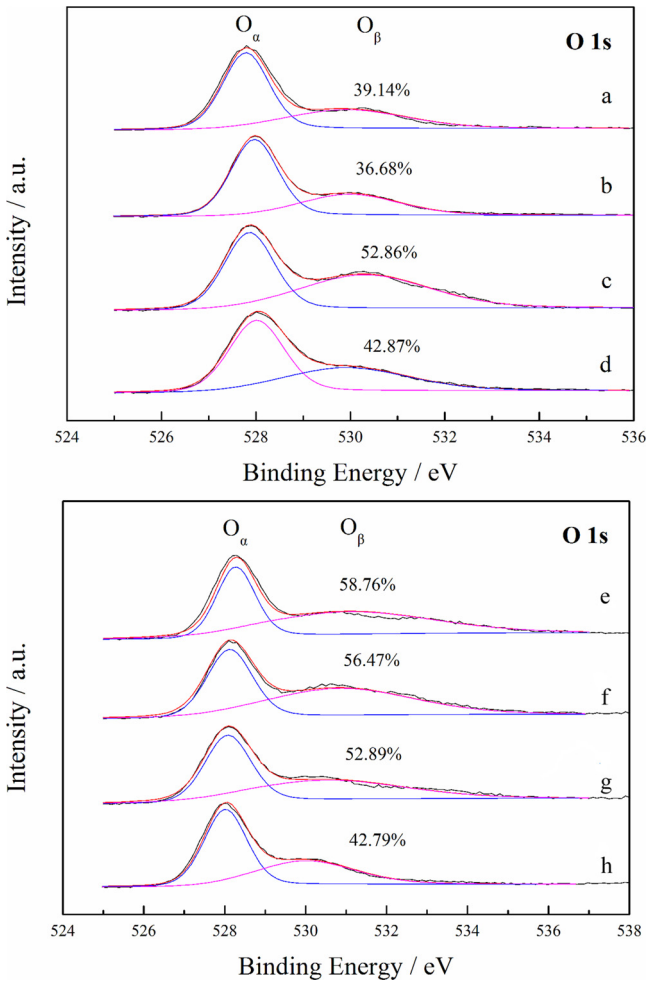

Fig. 3. O1s XPS spectra of (a) CeO_2-cube, (b) CeO_2-rod, (c) Mn_1Ce_3O-cube, (d) Mn_1Ce_3O-rod, (e) Pd/CeO_2-cube, (f) Pd/CeO_2-rod, (g) Pd/Mn_1Ce_3O-cube and (h) Pd/Mn_1Ce_3O-rod.

chemisorbed oxygen or the oxygen vacancy [29]. There is only a subtle difference of oxygen species between CeO_2-cube and CeO_2-rod supports. However, an obvious difference occurred with the morphology tuning after the doping of Mn. As the doping of Mn, the relative amount of O_β species for nanocube supports increased from 39.14% (Fig. 3(a)) to 52.86% (Fig. 3(c)), and from 36.68% (Fig. 3(b)) to 42.87% (Fig. 3(d)) for nanorod support, indicating that Mn dopants in solid solution are favorable for the formation of O_β species. The morphological effect observed on oxygen species was stronger for Mn_1Ce_3O than that for pure CeO_2, which shows that Mn dopants affect the oxygen species and strengthen the morphology effect. In fact, similar system was studied by simulation calculations [30], when Mn entered into the lattice of pure CeO_2, Mn3d–O2p gap state instead of Ce 4f and acted as an electron acceptor and donor during the first oxygen vacancy formation and O_2 replenishing, which helped to lower the formation energy of oxygen vacancies, therefore forming more O_β species. Moreover, nanocubes exposed the (100) plane could possess more O_β species than nanorods with (111) plane. This is probably because the (100) plane is more active than (111) plane, and the nanorods with the (111) plane need more energy to generate oxygen vacancy.

Compared with the supports, the addition of Pd resulted in a significant increase in the amount of O_β species for both Pd/CeO_2-cube and Pd/CeO_2-rod catalysts, and the amounts of O_β species increased to 58.76% (Fig. 3(e)) and 42.87% (Fig. 3(f)), whereas nearly the same amount of O_β species remains for Pd/Mn_1Ce_3O catalysts with cubic and rod-like shapes (Fig. 3(g) and (h)). It indicates that the loading of Pd

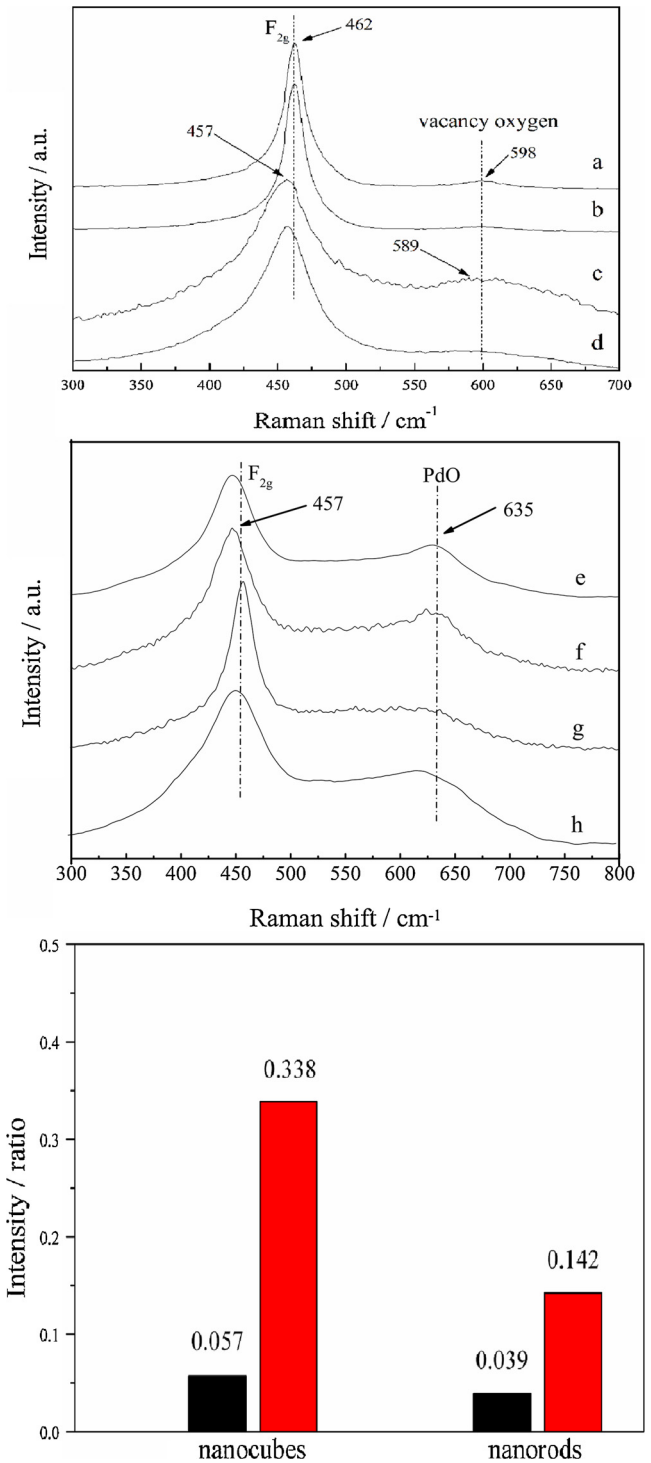

Fig. 4. Raman spectra of (a) CeO_2-cube, (b) CeO_2-rod, (c) Mn_1Ce_3O-cube, (d) Mn_1Ce_3O-rod, (e) Pd/CeO_2-cube, (f) Pd/CeO_2-rod, (g) Pd/Mn_1Ce_3O-cube and (h) Pd/Mn_1Ce_3O-rod, and peak intensity ratios of I_{598}/I_{462} over CeO_2 (black column) and Mn_1Ce_3O nanostructures (red column). (For interpretation of the references to color in this figure legend, the reader is referred to the web version of this article).

plays the similar tuning function to the doping of Mn. The loading of Pd also showed its influence on the amount of oxygen species. We inferred that both Pd and Mn are "dopants" for pure CeO_2, which improved the formation of oxygen vacancy. This observation is similar to the reported Pt/CeO_2 catalysts, wherein Pt could activate the surface Ce—O bond due to Pt-CeO_2 interaction [25]. Yang claimed that the interaction

between the palladium and the CeO_2 support enhanced the activity of the catalyst and explained that the adsorption of Pd on the O-bridge site enhanced the oxygen storage capacity (OSC) of CeO_2 [31].

The oxygen vacancy of the CeO_2 and Mn_1Ce_3O supports was further determined through Raman spectra (Fig. 4) [25]. A characteristic F_{2g} symmetry mode of CeO_2 phase can be clearly observed in the Raman spectra, located at approximately 462 cm^{-1}. The other weak peak, located at approximately 598 cm^{-1}, could be attributed to the defect-induced (D) mode. Furthermore, with the addition of Mn ions, the characteristic peak of Mn_1Ce_3O nanocubes red shifted from 462 cm^{-1} to 457 cm^{-1}, however, the characteristic peak of vacancy oxygen blue shifts from 598 cm^{-1} to 615 cm^{-1}. The intensity ratio I_{598}/I_{462} (I_{598} means the characteristic peak of oxygen vacancy induced by the presence of Ce^{3+} ions, I_{462} means the characteristic peak of the oxides) reflects the defect degree of nanostructures (Seen in Fig. 4). The I_{598}/I_{462} ratio estimated from the Raman spectra follows the order Mn_1Ce_3O-cube(0.338) > Mn_1Ce_3O-rod(0.142) > CeO_2-cube(0.057) > CeO_2-rod(0.039), which indicates that more oxygen vacancies existed in Mn_1Ce_3O nanomaterials compared to CeO_2 in view of the strong impact of Mn dopants on CeO_2 nanomaterials. The order of the intensity ratio I_{598}/I_{462} also showed a good amount of agreement with the results from O1s XPS spectra. Fig. 4(e)–(f) shows that the main PdO band at 635 cm^{-1} was present for the supported palladium catalysts except for the F_{2g} symmetry peak of CeO_2 at 457 cm^{-1} [32,33]. The weak peak intensity of the PdO band may stand for the partial formation of active PdO, while the chemical state of Pd species will be further characterized through XPS analysis. Considered that the characteristic peak of oxygen vacancy was not clear since it was close to the PdO band, the intensity ratio I_{598}/I_{462} after palladium supported is not integrated here.

XPS was employed to quantify the amount of active Pd^{2+} species in the prepared catalysts (Fig. 5). The XPS spectra of Pd 3d of catalysts were shown in Fig. 5, where palladium species existed mainly in Pd/CeO_2 and Pd/Mn_1Ce_3O catalysts was Pd°. The concentrations of active Pd^{2+} species of all catalysts were summarized in Table 1, which are 17.24%, 15.79%, 20.00% and 18.48% for Pd/CeO_2 nanocube, Pd/CeO_2 nanorod, Pd/ Mn_1Ce_3O nanocube and Pd/ Mn_1Ce_3O nanorod, respectively(As shown in Table 1). It was reported that the Pt^{2+}-CeO_2 interaction in a CeO_2-cube is stronger than the one in a CeO_2-rod [25]. But it appears that the metal-support interaction has only a little influence on the initial chemical state of palladium species, and may associate with the amount of oxygen vacancy according to the above analysis of O1s XPS spectra.

The activity of Pd supported catalysts was evaluated in the oxidative carbonylation of phenol for the synthesis of DPC and was summarized in Table 1. The activity was expressed in terms of reaction rate

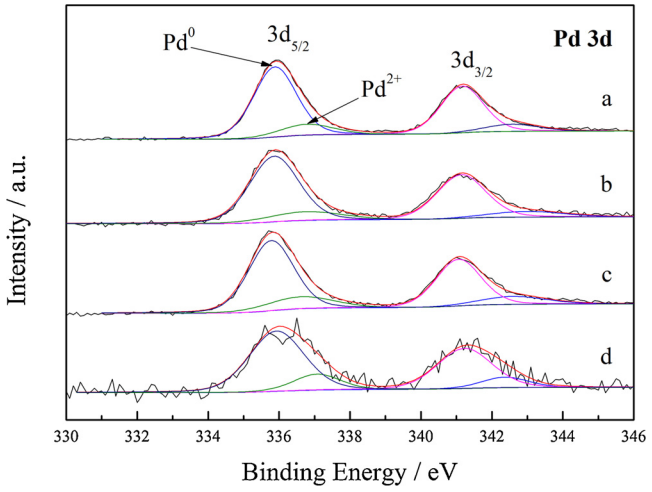

Fig. 5. Pd 3d XPS spectra of (a) Pd/CeO_2-cube, (b) Pd/CeO_2-rod, (c) Pd/Mn_1Ce_3O-cube and (d) Pd/Mn_1Ce_3O-rod.

($\times 10^{-3}$molDPC g^{-1} metal h^{-1}) and followed the order: Pd/Mn_1Ce_3O-cube (49.36) > Pd/Mn_1Ce_3O-rod (44.11) > Pd/CeO_2-cube (30.69) > Pd/CeO_2-rod (29.06). It appeared that the reaction rate increased as Mn was added. This shows that the additions of Mn led to the change of oxygen species, which is beneficial for the active Pd^{2+} species' catalysis of the oxidative carbonylation of phenol. In other words, O_β species are beneficial for catalytic performance. We propose that the role of O_β species (i.e. oxygen vacancy) is to make the reduction of palladium more difficult, since it has been reported that a stronger Pt^{2+}-CeO_2 interaction is more resistant for Pt reduction [25]. More O_β species means a stronger interaction, and a stronger interaction with active palladium species (Pd^{2+}) inhibits the reduction of palladium. Unlike the significant effect of additional Mn dopants on reaction rate, the morphology of catalysts has a subtle influence on reaction rate due to O_β species varying little with morphology. Comparatively speaking, Mn doping is more effective at promoting DPC formation than that of morphology tuning. Therefore, different amounts of Mn dopants were introduced in order to explore further the effects of Mn dopants on oxygen species and active Pd^{2+} species.

3.2. The effect of an increased amount of Mn dopants on catalytic performance

The surface area, the percentage of Pd^{2+} and Pd°, and the activity of Pd/CeO_2 and Pd/Mn_xCe_yO catalysts were summarized in Table 1 in order to determine the effects of Mn dopants on catalytic performance. The highest reaction rate of 73.64 × 10^{-3}molDPC g^{-1} metal h^{-1} was obtained for the Pd/Mn_3Ce_1O-cube catalyst. The effect of each factor on catalytic performance will be discussed along with characterization results.

Fig. 6 showed that XRD patterns of Pd/ Mn_xCe_yO catalysts with different amounts of Mn. The diffraction peaks of all catalysts appear at 2θ = 28.636°, 47.648°, and 56.386°, indicating the existence of CeO_2 (JCPDS No. 34-0394). For XRD patterns of the catalysts with rod and cube morphology, the formation of hollandite-type manganese oxides (JCPDS No. 42-1348) was observed when the molar ratio of Mn to Ce was 1/1 and 3/1. It has been reported that MnO_x would generate in Mn_xCe_yO mixed oxides at the molar ratio of Mn to Ce being larger than 1 [34]. Noticeably, the diffraction peak at 2θ = 35.512° that related to Mn_2O_3 (JCPDS No. 33-0900) was only found in Pd/Mn_1Ce_1O-cube and Pd/Mn_3Ce_1O-cube catalysts, which indicates that the structure of nanocubes is more active than that of nanorods and are easier to transform into Mn_2O_3. The presence of Mn_2O_3 in the two nanocubes could be attributed to the higher surface energy of nanocubes than that of nanorods. Fig. S2 shows the main morphology of nanocubes and nanorods retains and a little change happens due to the emergence of a new phase.

The relative amount of difference in oxygen species and the chemical state of active palladium species were studied by XPS analysis (Fig. 7) to compare with the results in Fig. 3. The amount of O_β species in Pd/Mn_3Ce_1O-cube catalysts is highest of 63.91% (Fig. 7(c)). An increase of the amount of O_β species, 55.56%, was also observed in Pd/Mn_3Ce_1O-rod when the molar ratio of Mn to Ce increased from 1/3 to 3/1. O1s XPS spectra shows that the increased amount of Mn improved the formation of more O_β species in spite of their morphology. Interestingly, an apparent change of Pd^{2+} concentration in Fig. 8 revealed that Mn dopants affect the interaction between palladium species and their supports. More active Pd^{2+} species turned up after more Mn dopants were added. The concentration of Pd^{2+} species follows the order Pd/Mn_3Ce_1O-cube (85.19%) > Pd/Mn_1Ce_1O-cube (70.79%) > Pd/Mn_1Ce_3O-cube (20.00%). The same trend as the nanocubes could be seen for nanorod catalysts as well, and the concentration of Pd^{2+} species was 18.48%, 68.02% and 79.34% in the sequence of Pd/Mn_1Ce_3O-rod, Pd/Mn_1Ce_1O-rod and Pd/Mn_3Ce_1O-rod catalysts. As we expected, the highest reaction rate of 73.64 × 10^{-3}molDPC g^{-1} metal h^{-1} was obtained for the Pd/Mn_3Ce_1O-cube catalyst in which more active Pd^{2+}

Table 1
Pd concentration and reaction rate of Pd/CeO_2 and Pd/Mn_xCe_yO catalysts.

Sample	$S_{BET}/(m^2\ g^{-1})$	Pd^{2+} (%)	Pd°(%)	Rate[a]($\times 10^{-3}$molDPC g^{-1} metal h^{-1})	Selectivity[b] (%)
Pd/CeO_2-cube	60.60	17.24	83.76	30.69	92.1
Pd/CeO_2-rod	68.89	15.79	83.21	29.06	94.8
Pd/Mn_1Ce_3O-cube	70.55	20.00	80.00	49.36	93.5
Pd/Mn_1Ce_3O-rod	75.15	18.48	81.52	44.11	94.2
Pd/Mn_1Ce_1O-cube	131.28	70.79	29.21	46.49	93.4
Pd/Mn_1Ce_1O-rod	119.57	68.02	31.98	38.98	95.0
Pd/Mn_3Ce_1O-cube	109.47	85.19	14.81	73.64	93.3
Pd/Mn_3Ce_1O-rod	110.03	79.34	20.66	72.47	91.7

[a] Calculated as: the mole of DPC in liquid products determined/(Pd mass in catalysts·reaction time).
[b] Calculated as: the mole of phenol that converted to DPC in liquid products/the total mole of phenol converted to DPC, 4-bromophenol, 3-phenoxyphenol and biphenyldiol in liquid products, and three different routes were proposed as shown in Scheme 1.

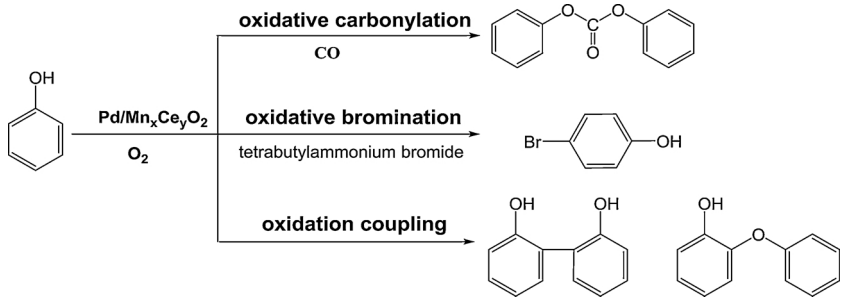

Scheme 1. Possible reaction pathways on Pd/Mn_xCe_yO catalysts.

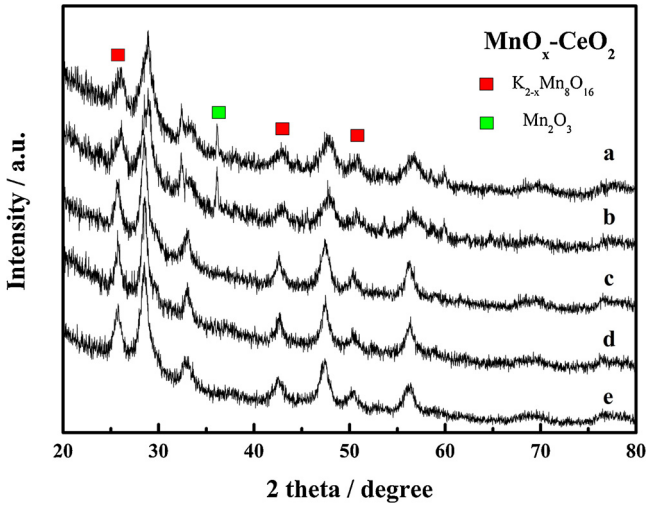

Fig. 6. XRD patterns of (a) Pd/Mn_1Ce_1O-cube, (b) Pd/Mn_3Ce_1O-cube, (c) Pd/Mn_1Ce_1O-rod, (d) Pd/Mn_3Ce_1O-rod and (e) the mixture of α-MnO_2 and CeO_2 (Mn:Ce = 1:3) as reference.

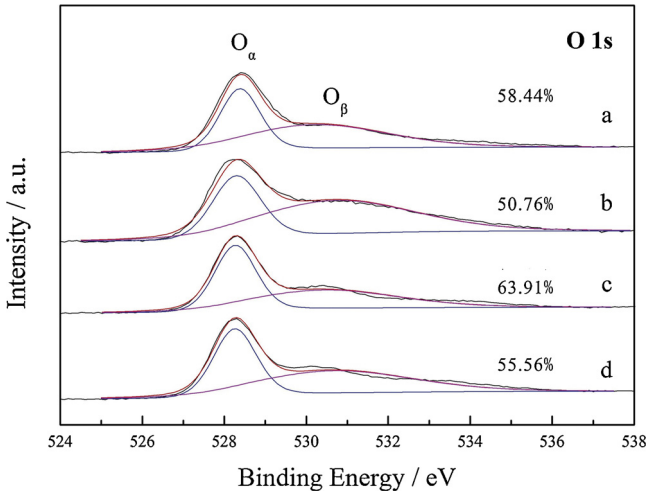

Fig. 7. O 1s XPS spectra of (a) Pd/Mn_1Ce_1O-cube, (b) Pd/Mn_1Ce_1O-rod, (c) Pd/Mn_3Ce_1O-cube and (d) Pd/Mn_3Ce_1O-rod.

species and more oxygen vacancies than other catalyst were presented (Seen in Table 1). Specific surface areas of all catalysts were measured as well, but poor correlation with reaction rate and selectivity was found. According to the reaction rate in Table 1, it appeared that the effect of morphology on catalytic performance is not stronger than that of the dopants. Meanwhile, the selectivity was hardly changed with the increased amount of Mn dopants.

The change in oxygen species and active Pd^{2+} species during the reaction was monitored and the used catalysts were analyzed through XPS spectra (Figs. S3 and S4). For Pd/Mn_xCe_yO catalysts, an obvious evolution from Pd^{2+} to Pd° as expected was not observed and active palladium species were almost the same as the initial state. It shows that the interaction between active Pd species and Mn_xCe_yO supports inhibits the reduction of active Pd^{2+} species to Pd°. However, the oxygen species in all catalysts differ from the initial state. It can be seen that more O_β species raised and lattice oxygen O_α was consumed during the reaction. In fact, such transformation of oxygen species in Pd/Mn-based catalysts was observed in our previous study, where we proposed that the lattice oxygen O_α involved the redox cycle [17,26]. In combination with the above results about oxygen species, we may deduce that O_β species, including oxygen vacancies, acted as intermediates to mitigate the reduction of active palladium species by the strong interaction between the noble metal and supports, while the lattice oxygen O_α involved the redox cycle of Pd°/Pd^{2+} in oxidative carbonylation of phenol to DPC. The synergistic effect of different oxygen species promoted the catalytic performance.

After all, we attempted to tune the oxygen species through the control of the morphology of the supports, but the corresponding catalytic performance during the oxidative carbonylation of phenol did not vary with the morphology significantly. The dopants appear to play a more important role in increasing the amount of O_β species. Moreover,

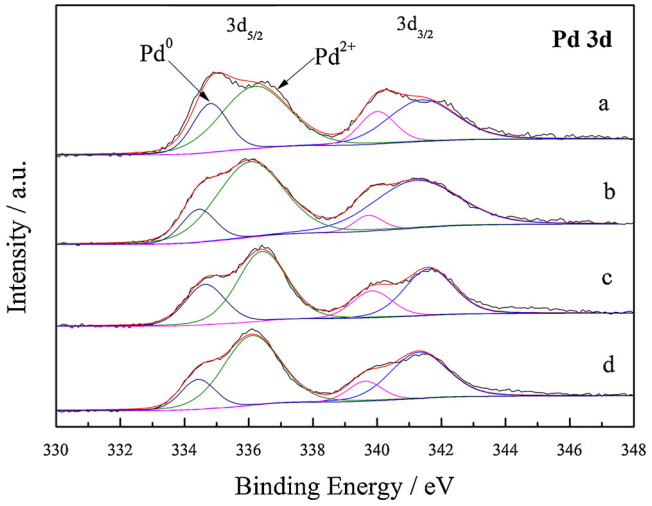

Fig. 8. Pd 3d XPS spectra of (a) Pd/Mn_1Ce_1O-cube, (b) Pd/Mn_3Ce_1O-cube, (c) Pd/Mn_1Ce_1O-rod and (d) Pd/Mn_3Ce_1O-rod.

the chemical state of active Pd^{2+} species presents more oxidative states with an increase in Mn dopants, which means a stronger interaction between active sites and supports. The improvement of catalytic activity for supported palladium catalysts is relatively more effective through the doping of Mn.

4. Conclusions

The effects of morphology and dopants on the catalytic performance of supported palladium catalysts for oxidative carbonylation of phenol were investigated. The various morphologies of the supports, which were nanocubes and nanorods of pure CeO_2 and Mn_xCe_yO mixed oxides, were designed by the hydrothermal method. It was found that the (100) crystal plane was exposed in the nanocube-based support but the (111) crystal plane was exposed in the nanorod-based support. Furthermore, it appears that the (100) plane exposed in nanocubes possesses more O_β species than the (111) plane exposed in nanorods. It is interesting that the O_β oxygen species are more sensitive to the doping of Mn than that to morphology tuning. The results indicated that the dopant plays a more important role than the morphology in Pd activity for the oxidative carbonylation of phenol. It appeared that the metal-support interaction may associate with the amount of oxygen vacancy. Comparatively speaking, doping is a more efficient method to control active oxygen species. The formation of initial active Pd^{2+} species for the oxidative carbonylation of phenol is easier during the catalyst preparation process as the amount of Mn dopants increases. The highest reaction rate of 73.64×10^{-3}mol DPC g^{-1} metal h^{-1} was obtained for Pd/Mn_3Ce_1O-cube catalyst due to more active Pd^{2+}species.

Acknowledgements

We are grateful for the financial support from National Natural Science Foundation of China (Grant No. 21276201) and Hubei Provincial Natural Science Foundation of China (Grant No. 2013CFA091). The authors will also thank the Opening Project of Hubei Key Laboratory of Lipid Chemistry and Nutrition (Grant No. 201505) and Wuhan Institute of Technology (Grant No. k201637) for its supports. Washington State University's work was also supported by the National Renewable Energy Laboratory Subcontract # AEV-6–52054-01 under Prime U.S. Department of Energy (DOE) Award # DE-AC36-08G028308, and the Joint Center for Aerospace Technology Innovation with the Bioproducts, Science & Engineering Laboratory and Department of Biological Systems Engineering at Washington State University. Dr. X. Yang was partially supported by CSC Scholarship for Overseas Studies.

Appendix A. Supplementary data

Supplementary material related to this article can be found, in the online version, at doi:https://doi.org/10.1016/j.mcat.2018.07.004.

References

[1] S.T. Gadge, B.M. Bhanage, RSC Adv. 4 (2014) 10367–10389.
[2] X.F. Wu, H. Neumann, M. Beller, ChemSusChem 6 (2013) 229–241.
[3] Y. Kim, K.Y. Choi, J. Appl. Polym. Sci. 49 (1993) 747–764.
[4] E.J. Pressman, B.F. Johnson, S.J. Shafer, Adv. Polycarbonates, American Chemical Society, 2005, pp. 3–22.
[5] J. Gong, X. Ma, S. Wang, Appl. Catal. A Gen. 316 (2007) 1–21.
[6] A.O. Biying, K.T. Yuanting, N.S. Hosmane, Y. Zhu, J. Organomet. Chem. 849 (2017) 195–200.
[7] K.I. Okuyama, J.I. Sugiyama, R. Nagahata, M. Asai, M. Ueda, K. Takeuchi, J. Mol. Catal. A Chem. 203 (2003) 21–27.
[8] H. Ishii, M. Goyal, M. Ueda, K. Takeuchi, M. Asai, Appl. Catal. A Gen. 201 (2000) 101–105.
[9] W.B. Kim, E.D. Park, C.W. Lee, J.S. Lee, J. Catal. 218 (2003) 334–347.
[10] H. Ishii, K. Takeuchi, M. Asai, M. Ueda, Catal. Commun. 2 (2001) 145–150.
[11] W. Xue, J. Zhang, Y. Wang, X. Zhao, Q. Zhao, Catal. Commun. 6 (2005) 431–436.
[12] K.J.L. Linsen, J. Libens, P.A. Jacobs, Chem. Commun. 22 (2002) 2728–2729.
[13] F. Guo-Zhi, L. Zhi-Qiang, H. Jiao, L. Tao, L. Guang-Xing, Chin. J. Inorg. Chem. 22 (2006) 1701–1705.
[14] Y. Yuan, Z. Wang, H. An, W. Xue, Y. Wang, Chin. J. Catal. 36 (2015) 1142–1154.
[15] L. Zhang, Y. He, X. Yang, H. Yuan, Z. Du, Y. Wu, Chem. Eng. J. 278 (2015) 129–133.
[16] L. Ronchin, A. Vavasori, E. Amadio, G. Cavinato, L. Toniolo, J. Mol. Catal. A Chem. 298 (2009) 23–30.
[17] Y. Hu, X. Yang, S. Cao, J. Zhou, Y. Wu, J. Han, Z. Yan, M. Zheng, Appl. Surf. Sci. 400 (2017) 148–153.
[18] J. Haber, Catal. Rev. 19 (1979) 1–41.
[19] X. Yang, J. Han, Z. Du, H. Yuan, F. Jin, Y. Wu, Catal. Commun. 11 (2010) 643–646.
[20] S. Chang, M. Li, Q. Hua, L. Zhang, Y. Ma, B. Ye, W. Huang, J. Catal. 293 (2012) 195–204.
[21] G.R. Li, T. Hu, G.L. Pan, T.Y. Yan, X.P. Gao, H.Y. Zhu, J. Phys. Chem. C 112 (2008) 11859–11864.
[22] X. Wang, J.a. Rodriguez, J.C. Hanson, D. Gamarra, A. Martínez-Arias, M. Fernández-García, J. Phys. Chem. B 110 (2006) 428–434.
[23] X.S. Huang, H. Sun, L.C. Wang, Y.M. Liu, K.N. Fan, Y. Cao, Appl. Catal. B Environ. 90 (2009) 224–232.
[24] H. Li, G. Qi, X. Tana, W. Zhang, W. Li, Shen, Catal. Sci. Technol. 1 (2011) 1677–1682.
[25] Y. Gao, W. Wang, S. Chang, W. Huang, ChemCatChem 5 (2013) 3610–3620.
[26] C. Yin, J. Zhou, Q. Chen, J. Han, Y. Wu, X. Yang, J. Mol. Catal. A Chem. 424 (2016) 377–383.
[27] W. Lu, Z. Du, H. Yuan, Q. Tian, Y. Wu, Chin. J. Chem. Eng. 21 (2013) 8–13.
[28] L. Yan, R. Yu, J. Chen, X. Xing, Cryst. Growth Des. 8 (2008) 1474–1477.
[29] D. Yu, W. Xingyi, L. Dao, D. Qiguang, J. Hazard. Mater. 188 (2011) 132–139.
[30] W. Cen, Y. Liu, Z. Wu, H. Wang, X. Weng, Phys. Chem. Chem. Phys. 14 (2012) 5769.
[31] Z. Yang, Z. Lu, G. Luo, K. Hermansson, Phys. Lett. A 369 (2007) 132–139.
[32] A. Baylet, P. Marécot, D. Duprez, P. Castellazzi, G. Groppi, P. Forzatti, Phys. Chem. Chem. Phys. 13 (2011) 4607–4613.
[33] G.W. Graham, A.E. O'Neill, D. Uy, W.H. Weber, H. Sun, X.Q. Pan, Catal. Lett. 79 (2002) 99–105.
[34] M. Machida, M. Uto, D. Kurogi, T. Kijima, Chem. Mater. 12 (2000) 3158–3164.